Sensitivity of Electrical Properties Tomography

Can we detect conductivity changes in magnetite-doped brain phantoms?

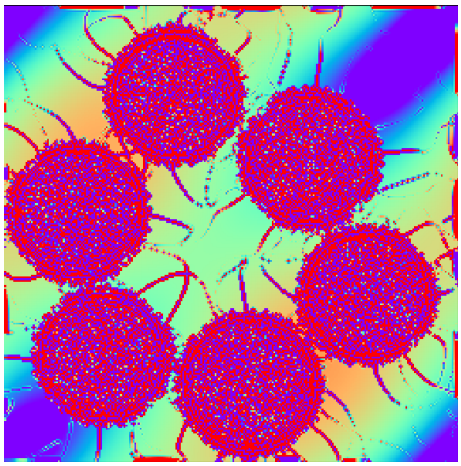

THESIS

submitted in partial fulfillment of the
requirements for the degree of

MASTER OF SCIENCE
in
PHYSICS

Author :	R. Overdevest, BSc.
Student ID :	1390481
Supervisor :	Dr. L. Bossoni
	Dr. W. Brink
	Prof.dr. A.G. Webb
2^{nd} corrector :	Prof.dr.ir. T.H. Oosterkamp

Leiden, The Netherlands, November 13, 2018

Sensitivity of Electrical Properties Tomography

Can we detect conductivity changes in magnetite-doped brain phantoms?

R. Overdevest, BSc.

Huygens-Kamerlingh Onnes Laboratory, Leiden University
P.O. Box 9500, 2300 RA Leiden, The Netherlands

November 13, 2018

Abstract

In this thesis we investigate conductivity changes due to magnetite in agarose gels mimicking grey brain matter. We use conventional MRI sequences to acquire B_1^+ phase maps. Using the homogeneous Helmholtz equation and the B_1^+ phase-only approximation, we reconstruct conductivity maps. The current sensitivity of the reconstructions is too low to detect conductivity changes due to magnetite nanoparticles in the concentration found in the brain of Alzheimer's disease patients. Nevertheless, we have promising indications that we have been able to observe a change in the standard deviation of the conductivity due to the presence of magnetite.

Contents

Chapter 1

Introduction

Alzheimer's disease, the world leading cause of dementia, is a condition that causes memory deterioration, influences behavior and hinders every day activities. The World Health Organization[1] estimates that Alzheimer's disease contributes to 60-70% of all positively diagnosed dementia cases worldwide.

How to diagnose Alzheimer's disease in a living human being? This is a question that still has no definitive answer. Alzheimer's disease is being diagnosed either post-mortem or based on the person's medical history, the history of their relatives and observations of their behavior. A biomarker that can be used for diagnosis of Alzheimer's disease in vivo is surely needed.

In 1953, Goodman[2] already linked unnatural concentrations of iron in the brain with Alzheimer's disease. Since then, iron accumulation in the human brain has been associated with all kinds of neurodegenerative diseases like Parkinson's disease, Huntington's disease and many others.

Magnetite (Fe_3O_4) and ferrihydrite[1] are two iron-oxide minerals which have been observed in the brain of Alzheimer's disease patients, with altered concentrations[4]. It has been suggested that an increase of the iron concentration in the brain with respect to the iron concentration of the healthy human brain increases the likelihood of Alzheimer's disease.

In 2017 Nurdin[5] reported electric conductivity enhancements of maghemite (γ-Fe_2O_3) nanofluids. When increasing the particle volume fraction of magnetite in the nanofluid, an almost linear increase in conductivity was observed. Since maghemite is similar to magnetite, both in structure and magnetic properties, it is not unreasonable to expect a similar

[1] Ferrihydrite is the mineral form in which iron is stored in ferritin[3], a protein that stores and releases iron in the brain.

behavior for magnetite nanofluids. Additionally, magnetite could even be found in the brain in an oxidized form, i.e. maghemite[4].

It has been proposed that magnetite, and other forms of iron in the brain, might be a potential biomarker for diagnosing Alzheimer's disease in the human brain in vivo[6]. Additionally, the concentration of magnetite locally influences the electrical conductivity in the brain. Now all we need is a way to observe this potential electrical conductivity change near iron clusters in the brain.

Electrical Properties Tomography (EPT) is a method that allows measurement of local dielectric properties of tissue using standard MRI sequences. This method is based on measuring the complex component of the transmit field B_1^+. Using the homogeneous Helmholtz equation, the B_1^+map can be used to reconstruct a conductivity map. In 2012 van Lier et al. proposed an improvement on the existing EPT protocol. Their method, which has some constraints, only requires a B_1^+phase map to reconstruct an electric conductivity map.

The goal of this project is to test if the EPT method can be used to differentiate a sample mimicking a healthy brain's grey matter from another containing magnetite nanoparticles in a concentration similar to that found in the brain cortex of Alzheimer's disease patients[6][7][8]. For this we produced phantoms of agarose: a gel which has similar proton density and relaxation rates as the brain cortex, and add different concentrations of magnetite. We use pre-existing MRI protocols to extract the transceive phase map, which we can use to reconstruct an electrical conductivity map in post-processing.

Chapter 2

Theory

We start this chapter by introducing the basics of MRI and the reciprocity theorem. We introduce the theory on which the conductivity reconstruction from the B_1^+phase is based and discuss how to retrieve the transmit phase from the transceive phase, which is required for the conductivity reconstruction. Also, we discuss how to calculate the numerical Laplacian emerging in the expression for the conductivity and how it can be modified to improve the noise-robustness of the kernel. To close off the theory chapter, we introduce the concept of Gibbs-ringing and discuss a way to minimize it in the phase maps used for the conductivity reconstruction.

2.1 MRI Basics & the Reciprocity Theorem

MRI (Magnetic Resonance Imaging) is a technique which uses an external static magnetic field to induce a splitting of the energy state. The protons can either align parallel or anti-parallel to the magnetic field and there is a small population difference between these two states. Using RF (Radio Frequency) pulses, protons can be excited from the lower energy state to the other. Only the protons that undergo this transition are of relevance for MRI. These protons will relax back to the lower energy state by emitting photons, which can be detected by the receive coils present in the scanner.

Now we will go more in depth and describe the principles of MRI (and NMR) using a semiclassical approach, which is sufficient for the description of the effects that are of importance for this thesis.

Let us consider a spin ensemble inside an electromagnetic field. All the spins are characterized by a nuclear spin **I** not equal to zero. For example, the nuclear spin of a hydrogen nuclei is: $I = \frac{1}{2}$. **I** is linked to the nuclei's

momentum by:

$$\mathbf{m} = \gamma \cdot \mathbf{I} \tag{2.1}$$

where γ is the gyromagnetic ratio, which is unique for each nucleus. In the case of hydrogen nuclei: $\gamma \approxeq 42.57 \frac{\text{MHz}}{\text{T}}$.

When we apply a static homogeneous external magnetic field $\mathbf{B}_0$ to the ensemble, by virtue of the Zeeman effect[9], the energy level of $\mathbf{I}$ splits into $2I + 1$ discrete energy levels. An $I = \frac{1}{2}$ system splits into two distinct spin states: $\frac{1}{2}$ and $-\frac{1}{2}$. By convention $\mathbf{B}_0$ is oriented along the z-axis. Thus the two spin states adopt either the parallel or anti-parallel orientation with an angular orientation of $\Omega_0 \approxeq 54.7^{\text{o}}$ with respect to the z-axis, as depicted in Figure 2.1.

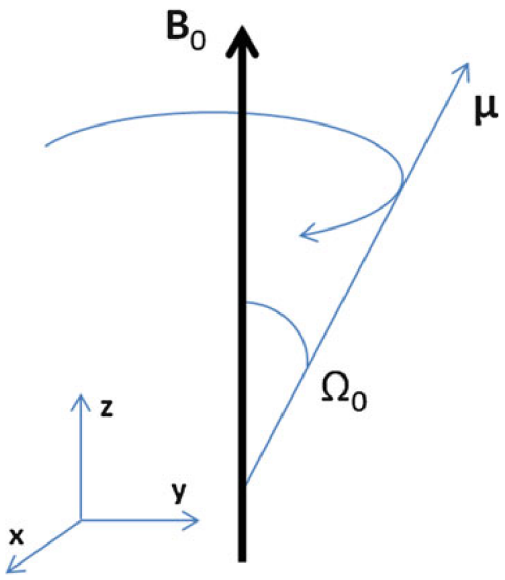

Figure 2.1: *Precession of the magnetic momentum* $\boldsymbol{\mu}$ *about the* $\mathbf{B_0}$ *vector under an angle* $\mathbf{\Omega_0}$*. Image reproduced from Ning et al.[10].*

There is an energy difference $\Delta E = \gamma \hbar B_0$ between the two spin states. A transition from one energy level to another is possible by either absorption or emission of a photon, e.g. receiving or sending an electromagnetic wave with energy equal to the energy difference of the levels:

$$\Delta E = \hbar \omega_0, \quad \omega_0 = \gamma B_0 \tag{2.2}$$

where ω_0 is the Larmor frequency.

Usually, objects under investigation contain many nuclear spins. Therefore the distribution of the energy levels is governed by Boltzmann statistics. The probability of a nuclear spin having a certain energy is determined by the Boltzmann factor $e^{-\frac{\Delta E}{k_B T}}$, where k_B is Boltzmann's constant and T is the temperature. If the system is at equilibrium, the lower energy level (parallel) is slightly[1] more populated than the higher level (anti-parallel). Therefore, whenever a sample is placed in a uniform field $\mathbf{B}_0$, a net magnetization $\mathbf{M} = \sum \mathbf{m}$ along the direction of the field is induced in the sample. Also, a torque on the net magnetization $\mathbf{M}$, resulting from the interaction between the $\mathbf{B}_0$ field and the resulting magnetization, causes the magnetization to precess about its axis at the Larmor frequency ω_0 (see Figure 2.1). This precession is governed by the differential equation:

$$\frac{d}{dt}\mathbf{M}(t) = \gamma \mathbf{M}(t) \times \mathbf{B}_0 \tag{2.3}$$

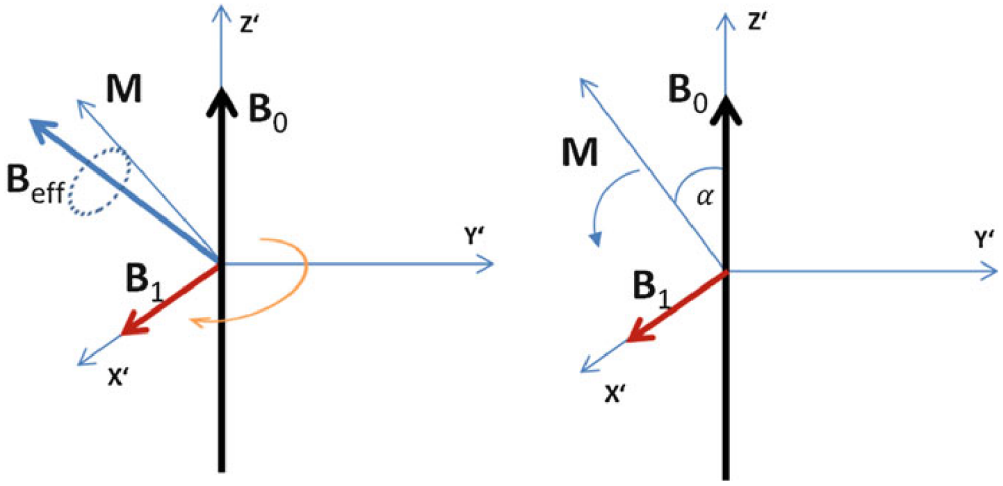

Figure 2.2: *Left: magnetization* $\boldsymbol{M}$ *precessing about the effective magnetic field* $\boldsymbol{B}_{eff}$ *in the rotating frame. Right: flipping of the magnetization under an angle* α *by applying the transverse RF field* $\boldsymbol{B}_1$*. Image reproduced from Ning et al.[10].*

Now we introduce a rotating coordinate frame which is aligned with the $\mathbf{B}_0$ field, as depicted in Figure 2.2. We also introduce a second magnetic field denoted by $\mathbf{B}_1$, which is linearly polarized in the x direction. The effective magnetic field $\mathbf{B}_{eff}$ in the static (not rotating) frame is equal to:

[1] This small population difference is the cause for the relatively low sensitivity of MRI. It can be increased by increasing B_0, which is a major reason for increasing the field strength used for MRI.

$$\mathbf{B}_{eff} = \mathbf{B}_1 + \frac{\omega_0}{\gamma}\mathbf{e}_z \tag{2.4}$$

$\mathbf{B}_1$ is an oscillating RF field:

$$\mathbf{B}_1 = A\mathbf{e}_x cos(\omega t) = \mathbf{B}_1^+ + \mathbf{B}_1^- \tag{2.5}$$

$$\mathbf{B}_1^+ = \frac{1}{2}A\left(\mathbf{e}_x cos(\omega t) - \mathbf{e}_y sin(\omega t)\right) \tag{2.6}$$

$$\mathbf{B}_1^- = \frac{1}{2}A\left(\mathbf{e}_x cos(\omega t) + \mathbf{e}_y sin(\omega t)\right) \tag{2.7}$$

$\mathbf{B}_1^+$ is rotating clockwise while $\mathbf{B}_1^-$ is rotating counterclockwise. We can express these in the rotating reference frame[11]:

$$\mathbf{B}_1^+ = \frac{1}{2}A\mathbf{e}_{x'} \tag{2.8}$$

$$\mathbf{B}_1^- = \frac{1}{2}A\left(\mathbf{e}_{x'} cos(2\omega_0 t) + \mathbf{e}_{y'} sin(2\omega_0 t)\right) \tag{2.9}$$

The effective magnetic field in the rotating reference frame becomes:

$$\mathbf{B}_{eff} = \frac{1}{2}A\mathbf{e}_{x'} + \left(B_0 - \frac{\omega_0}{\gamma}\right)\mathbf{e}_z \tag{2.10}$$

Since the system is on resonance, $\omega = \omega_0$, the external field $\mathbf{B}_0$ no longer influences the motion, i.e. the z component in Equation 2.10 is equal to 0. The magnetization will rotate due to a torque aligned to $\mathbf{B}_{eff} = \frac{1}{2}A\mathbf{e}_{x'}$. This results in a flipping of the magnetization under an angle α away from the equilibrium, as depicted in Figure 2.2. For a simple block-shaped RF pulse, it's length determines the total flipping angle.

Here we have demonstrated that the clockwise rotating component of $\mathbf{B}_1$ affects the magnetization vector $\mathbf{M}$. A similar argument, where the rotating frame rotates in the opposite direction, can be used to show that $\mathbf{B}_1^-$ has no effect on the magnetization. Therefore, for a linearly polarized RF $\mathbf{B}_1$-field only half of the energy is used for flipping the magnetization vector.

To use the whole energy to flip the magnetization we can use the clockwise rotating field:

$$\mathbf{B}_1^+ = A\left(\mathbf{e}_x cos(\omega t) + \mathbf{e}_y sin(\omega t)\right) \tag{2.11}$$

This field creates an effective field:

$$\mathbf{B}_{eff} = A\mathbf{e}_{x'} \tag{2.12}$$

adding twice the energy that was otherwise added to the system.

After flipping of the magnetization due to the RF $\mathbf{B}_1$ pulse the magnetization is precessing in the xy-plane. However, this state will not last indefinitely. Due to relaxation effects, the magnetization will return to align with $\mathbf{B}_0$. This relaxation is characterized by two relaxation times: T_1 and T_2. T_1 governs the longitudinal relaxation and is due to interactions of the spins with the lattice. T_2 describes the energy transfer between the spins, which causes a loss of phase coherence[2]. Both times depend on the material and the field strength used. The time evolution of a spin system after excitation by an RF-pulse are characterized by the Bloch equations:

$$\frac{dM_{x,y}}{dt} = \gamma \left(\mathbf{M} \times \mathbf{B}\right)_{x,y} - \frac{M_{x,y}}{T_2} \tag{2.13}$$

$$\frac{dM_z}{dt} = \gamma \left(\mathbf{M} \times \mathbf{B}\right)_z - \frac{M_z - M_0}{T_1} \tag{2.14}$$

Let us consider Equation 2.13 when a $\mathbf{B}_1$-field is applied along the x direction. For times t much less than T_2 Equation 2.13 can be written (using the right hand notation) as[11]:

$$\frac{dM_x^+}{dt} \approx \gamma B_{1,y}^+ M_z \tag{2.15}$$

$$\frac{dM_y^+}{dt} \approx -\gamma B_{1,x}^+ M_z \tag{2.16}$$

Now we use the small flip angle approximation ($\alpha \leq 10^o$), for which $M_z \approx M_0$. Then we find:

$$M_x^+ \approx \gamma B_{1,y}^+ M_0 \tau \tag{2.17}$$

$$M_y^+ \approx -\gamma B_{1,x}^+ M_0 \tau \tag{2.18}$$

where τ is the duration of the RF pulse.

The total magnetization M^+ is given by[11]:

$$M^+ = M_x^+ + iM_y^+ \approx -i\gamma\tau M_0 B_1^+ \tag{2.19}$$

[2]Actually, there is a third relaxation time T_2^*, which combines T_2 and the effects of local B_0 inhomogeneities.

This equation shows that for small flip angles the transverse magnetization is proportional to the B_1 field strength, up to a -90^o rotation due to the $'-i'$ multiplier.

Using a similar argument in a frame with an opposite rotation, it can be shown that the signal ξ received by a pickup coil is equal to[11]:

$$\xi = 2\omega M^+ \left(B_1^-\right)^* \tag{2.20}$$

where the asterisk denotes complex conjugation.

These relations are part of the principle of reciprocity. Here we have shown that for MR measurements the measured signal will be influenced by both the transmit field as well as the receive sensitivity.

2.2 Conductivity Reconstruction using the Helmoltz Equation

To obtain an expression for the conductivity (σ) in terms of the transmit B_1^+field we need to recall the Helmholtz equation for the magnetic field. For this, we start from Ampère's and Faraday's law in matter:

$$-\nabla \times H + J^{con} + \frac{\partial D}{\partial t} = -J^{ext} \tag{2.21}$$

$$\nabla \times E + \frac{\partial B}{\partial t} = -K^{ext} \tag{2.22}$$

where J^{ext} & K^{ext} are the electric and magnetic current densities, H & E are the magnetic and electric field strength, J^{con} is the electric conduction current density and D & B are the electric and magnetic flux densities. Recalling that the above fields are planar waves we can write:

$$E(x,t) = \Re(\hat{E}(x,\omega)e^{i\omega t}) \tag{2.23}$$

$$H(x,t) = \Re(\hat{H}(x,\omega)e^{i\omega t}) \tag{2.24}$$

$$\hat{J}^{con}(x,\omega) = \hat{\sigma}(x,\omega)\hat{E}(x,\omega) \tag{2.25}$$

$$\hat{D}(x,\omega) = \hat{\epsilon}(x,\omega)\hat{E}(x,\omega) \tag{2.26}$$

$$\hat{B}(x,\omega) = \hat{\mu}(x,\omega)\hat{H}(x,\omega) \tag{2.27}$$

where i denotes the imaginary unit, ω the angular frequency, $\hat{\sigma}$ the conductivity, $\hat{\epsilon}$ the permittivity, $\hat{\mu}$ the permeability, $\Re$ the real part of its

complex argument and x is a three dimensional vector specifying the location of the field ($x \in \mathbb{R}^3$). Here we have used the hat notation to denote the frequency domain representation of the quantities.

Combining Equations 2.21 to 2.27 we get the following pair of equations:

$$-\nabla \times \hat{H} + \hat{\sigma}\hat{E} + i\omega\hat{\epsilon}\hat{E} = -\hat{J}^{ext} = -\nabla \times \hat{H} + \hat{\eta}\hat{E} \tag{2.28}$$

$$\hat{\eta} = \hat{\sigma} + i\omega\hat{E} \tag{2.29}$$

$$\nabla \times \hat{E} + i\omega\hat{\mu}\hat{H} = -\hat{K}^{ext} = \nabla \times \hat{E} + \hat{\zeta}\hat{H} \tag{2.30}$$

$$\hat{\zeta} = i\omega\hat{\mu} \tag{2.31}$$

For convenience of writing we drop the hats from now on, while keeping in mind that all quantities are still represented in the frequency domain. Let us assume there are no external electric and magnetic currents in the region of interest, i.e. J^{ext} and K^{ext} are equal to zero. This results in the following set of equations:

$$\nabla \times H = \eta E \tag{2.32}$$

$$\nabla \times E = -\zeta H \tag{2.33}$$

Now by taking the cross product of both sides of Equation 2.32 we obtain:

$$\nabla \times E = \frac{1}{\eta}(\nabla \times (\nabla \times H)) = -\zeta H \tag{2.34}$$

Using the cross product identity $\nabla \times (\nabla \times A) = \nabla(\nabla \cdot A) - \nabla^2 A$ we can rewrite Equation 2.34 in the following way:

$$-\zeta\eta H = \nabla \times (\nabla \times H) = \nabla(\nabla \cdot H) - \nabla^2 H = -\nabla^2 H \tag{2.35}$$

where the last equality is due to the following: taking the dot product of both sides of Equation 2.33 we get: $\nabla \cdot (\nabla \times E) = -\zeta \nabla \cdot H = 0$, where the last equality always holds, since the divergence of the curl is always equal to zero.

Since B is proportional to H, we can re-write the last equation as the following:

$$\nabla^2 B + k^2 B = 0, \quad k^2 = \omega^2\epsilon\mu - i\omega\mu\sigma \tag{2.36}$$

which is the homogeneous Helmholtz equation.

Rewriting this equation in terms of the circularly polarized transmit magnetic field $B_1^+ = \frac{B_x + iB_y}{2}$ yields the final Helmholtz equation:

$$\frac{\nabla^2 B_1^+}{B_1^+} = -k^2 \tag{2.37}$$

Solving for ϵ and σ we find:

$$\epsilon = -\Re\left(\frac{\nabla^2 B_1^+}{B_1^+}\right)\frac{1}{\mu\omega^2} \tag{2.38}$$

$$\sigma = \Im\left(\frac{\nabla^2 B_1^+}{B_1^+}\right)\frac{1}{\mu\omega} \tag{2.39}$$

Equation 2.39 is the formal expression of σ in terms of $B_1^+$and therefore it is the central equation of this thesis. Since the conductivity reconstruction is based on the homogeneous Helmholtz equation this result is only valid in piecewise constant dielectric regions.

2.3 The B_1^+Phase-only Approximation

Equation 2.39 allows us to reconstruct the conductivity from the complex B_1^+field. The phase (ϕ_+) and magnitude ($|B_1^+|$) of the complex $B_1^+ = |B_1^+|e^{i\phi_+}$ field require separate measurements. If we are only interested in a sufficient conductivity map, we can further simplify Equation 2.39. If the $|B_1^+|$ field is well-behaved we can, under certain constraints, directly reconstruct the conductivity from the B_1^+phase only.

To demonstrate this, we start from the homogeneous Helmholtz equation (Equation 2.37). We separate phase and magnitude of the complex B_1^+field:

$$B_1^+ = |B_1^+|e^{i\phi_+} \tag{2.40}$$

and combine Equations 2.40 and 2.37:

$$\frac{\nabla^2|B_1^+|}{|B_1^+|} + \frac{2\nabla|B_1^+|\nabla e^{i\phi_+}}{|B_1^+|e^{i\phi_+}} + \frac{\nabla^2 e^{i\phi_+}}{e^{i\phi_+}} = -k^2, \quad k^2 = \omega^2\epsilon\mu - i\omega\mu\sigma \tag{2.41}$$

To obtain an expression for σ we take the imaginary part of both sides to find:

$$\Im\left(\frac{2\nabla|B_1^+|\nabla e^{i\phi_+}}{|B_1^+|e^{i\phi_+}}+\frac{\nabla^2 e^{i\phi_+}}{e^{i\phi_+}}\right)\frac{1}{\mu_0\omega}=\sigma \tag{2.42}$$

where $\frac{\nabla^2|B_1^+|}{|B_1^+|}$ has dropped out since it is real valued.

If we assume that the spatial variation of $|B_1^+|$ is small ($\nabla|B_1^+|$ is sufficiently small) we obtain the final expression of σ, which is now only a function of the phase of the B_1^+ field:

$$\Im\left(\frac{\nabla^2 e^{i\phi_+}}{e^{i\phi_+}}\right)\frac{1}{\mu_0\omega}=\sigma \tag{2.43}$$

Here we have come across the first constraint for the conductivity reconstruction solely based on the B_1^+ phase: the variation in the magnitude of the B_1^+ field should be sufficiently small compared to the variation in its phase. This requirement is usually met in a subject placed in the center of a volume transmit coil and when that subject contains sufficiently large homogeneous regions.

A conductivity reconstruction based on Equation 2.43 requires a measurement of the B_1^+ phase, which is the difference in phase acquired by the RF-field propagating from the source into the sample. By virtue of reciprocity[3], MR phase measurements are inherently influenced by both transmit phase contributions as well as phase components attributed to the receive sensitivity. We therefore always measure the sum of both, represented by the transceive phase $\phi_\pm$ in the following way:

$$\phi_\pm(r)=\phi_+(r)+\phi_-(r) \tag{2.44}$$

The measured transceive phase is not the phase that we should use for the conductivity reconstruction. Van Lier et al.[12] showed that for some situations[4] there is a simple relation between the measured transceive phase and the transmit phase:

$$\phi_\pm(r)=2\phi_+(r) \tag{2.45}$$

This is the second constraint for the B_1^+ phase only conductivity reconstruction.

[3] See Section 2.1.

[4] For example this relation holds for a dielectrically homogeneous lossy cylinder using quadrature excitation and reception with the same coils[12].

Finally the measured phase ϕ_S does not only consist of the transceive phase, it is also influenced by B_0 inhomogeneities, chemical shifts and eddy currents[5]:

$$\phi_S(r, TE) = \phi_{\pm}(r) - \omega_{off-res}(r)TE + \int_0^{TE} \gamma B_e dt \tag{2.46}$$

The off-resonance phase contributions are linear in TE, the echo time of the pulse sequence. Therefore $\omega_{off-res}$ can be determined by measuring twice using different echo times.

The eddy current contribution depends on the polarity of the gradients. To cancel out the eddy current part, we take the average of two independently acquired B_1^+phase maps. The two maps are identical, except for the gradients which have opposite polarity. Averaging these two independently acquired phase maps cancels the third term in Equation 2.46. This results in the final expression for the transmit phase ϕ_+:

$$\phi_+ = \frac{\phi_{S,+} + \phi_{S,-}}{4} \tag{2.47}$$

where $\phi_{S,+}$ is the phase measured with a positive gradient and $\phi_{S,-}$ is the phase measured with the opposite gradient[13].

2.4 Calculating the Laplacian

The expression for the conductivity (Equation 2.43) contains a term involving the Laplacian of the B_1^+phase. A phase map of a single slice consists of an N x N pixels array, where the spacing between pixels, also known as resolution[6], heavily influences any numerical derivative calculation. A typical value for the resolution of the phase maps in this thesis is about 1 mm/pixel, which influences the sensitivity of the Laplacian. A higher resolution would result in a smoother reconstruction[7]. Moreover, noise in the phase maps is amplified in derivative calculations.

To combat the smoothness and potential noise problem we implemented three different kernels for the numerical Laplacian calculation: $k_{2D-small}$,

[5]Eddy currents are loops of current in the metallic structure of the MRI bore which are induced by time-varying magnetic fields due to Faraday's law of induction. In turn, eddy currents produce a magnetic field opposing the source magnetic field.

[6]The resolution of an image is defined as the field of view (FOV) divided by the image size.

[7]A too hig resolution would negatively impact the SNR of the phase map. Averaging many images would be an easy way to combat this, but is very time consuming.

$k_{2D-large}$ and k_{3D}. Two of these kernels apply a smoothening filter as well as a second derivative calculation to a phase map. All three kernels use the finite difference approximation of the continuous Laplace differential operator to calculate the numerical Laplacian. The Laplacian is then calculated by convolving the phase map with the chosen kernel.

$k_{2D-small}$ and $k_{2D-large}$ are 2D kernels, which means they calculate second order derivatives only in-plane: $\nabla^2_{2D} = \frac{d^2}{dx^2} + \frac{d^2}{dy^2}$. k_{3D} is a 3D kernel, therefore it calculates second order derivatives both in-plane as well as through the plane: $\nabla^2_{3D} = \frac{d^2}{dx^2} + \frac{d^2}{dy^2} + \frac{d^2}{dz^2}$. $k_{2D-large}$ and k_{3D} were constructed by Holoborodko[14].

$k_{2D-small}$ is the bare finite difference implementation of the 3 x 3 Laplacian kernel, meaning it does nothing to improve upon any smoothness and noise problems. Its explicit form is:

$$k_{2D-small} = \frac{1}{a_{xy}^2} \begin{bmatrix} 0 & 1 & 0 \\ 1 & -4 & 1 \\ 0 & 1 & 0 \end{bmatrix}$$

where a_{xy} denotes the resolution of the image in plane.

$k_{2D-large}$ is a noise-robust 3 x 7 kernel:

$$k_{2D-large} = \frac{1}{32a_{xy}^2} \begin{bmatrix} 0.5 & 1 & -0.5 & -2 & -0.5 & 1 & 0.5 \\ 1 & 2 & -1 & -4 & -1 & 2 & 1 \\ 0.5 & 1 & -0.5 & -2 & -0.5 & 1 & 0.5 \end{bmatrix}$$

This kernel performs a second order derivative and a smoothening operation along its largest axis: the 3 x 7 kernel calculates $\frac{d^2}{dx^2}$. To calculate $\frac{d^2}{dy^2}$, the kernel needs to be transposed (which results in a 7 x 3 kernel). The separate second order derivatives need to be summed to obtain the full Laplacian.

k_{3D} is a 7 x 7 x 5 kernel, which uses a 7 x 3 x 3 kernel ($k_{3D-large}$) to calculate the in plane (x and y) second order derivatives and a 5 x 3 x 3 kernel ($k_{3D-small}$) to calculate the second order derivative across the planes (z). Just as with the $k_{2D-large}$ kernel, the 7 x 3 x 3 kernel needs to be transposed to calculate the second order derivative along the y direction. Again, the separate second order derivatives need to be summed to obtain the full Laplacian.

Denoting the third dimension (z) with index i, we can write the explicit form of $k_{3D-large,i}$ and $k_{3D-small,i}$:

$$k_{3D-large,2} = \frac{1}{64a_{xy}^2}\begin{bmatrix} 0.5 & 1 & -0.5 & -2 & -0.5 & 1 & 0.5 \\ 1 & 2 & -1 & -4 & -1 & 2 & 1 \\ 0.5 & 1 & -0.5 & -2 & -0.5 & 1 & 0.5 \end{bmatrix}$$

$$k_{3D-large,1} = k_{3D-large,3} = \frac{1}{2}k_{3D-large,2}$$

$$k_{3D-small,1} = k_{3D-small,5} = \frac{1}{64a_z^2}\begin{bmatrix} 0.25 & 0.5 & 0.25 \\ 0.5 & 1 & 0.5 \\ 0.25 & 0.5 & 0.25 \end{bmatrix}$$

$$k_{3D-small,3} = -2\,k_{3D-small,1}$$

$$k_{3D-small,2} = k_{3D-small,4} = \begin{bmatrix} 0 & 0 & 0 \\ 0 & 0 & 0 \\ 0 & 0 & 0 \end{bmatrix}$$

where a_z^2 denotes the resolution in the z direction.

The prefactor of $\frac{1}{32}$ for $k_{2D-large}$ and $\frac{1}{64}$ for k_{3D} were determined by Holoborodko[14] and are necessary for keeping the smoothening operation normalized.

For the boundary voxels of the image volume, zero-padding is used. This means that every neighbor missing in the calculation of the convolution for a boundary voxel is set to zero. This makes the first and last slice of a reconstruction using the k_{3D} kernel unreliable. For $k_{2D-small}$ and $k_{2D-large}$ the boundary pixels usually do not include the sample. Therefore, the zero-padding will not influence the reconstructions in important regions of the reconstruction.

2.5 Gibbs-ringing

MR images are not acquired in real space, they are acquired in k-space. The value of a certain pixel is reconstructed in real space using the Fourier transform.

Gibbs-ringing[8] is an artifact that may arise in MR images. It usually appears as multiple parallel lines near high contrast interfaces. Its origin lies in the finite number of Fourier expansion coefficients that can be acquired to reconstruct the image value of a certain pixel:

$$I(x) = \frac{1}{N}\sum_{k=0}^{N-1} c(k)e^{\frac{-2\pi ikx}{N}} \tag{2.48}$$

[8]Gibbs-ringing is also known as Gibbs artifact, Gibbs truncation and spectral leakage.

where $I(x)$ denotes the value of the pixel at index x and $c(k)$ are the N Fourier expansion coefficients. Whenever the coefficients $c(k)$ do not decay to zero fast enough with increasing k the Gibbs-ringing artifact appears in the image. Especially when there is a sharp transition in the image all higher frequency components of the Fourier series are required to reconstruct the pixel value accurately.

The "truncation" of k-space corresponds to a multiplication of the total unbounded k-space with a rectangular window. In the image domain this is equivalent to a convolution with a sinc function, which will cause oscillations near sharp transitions in the image.

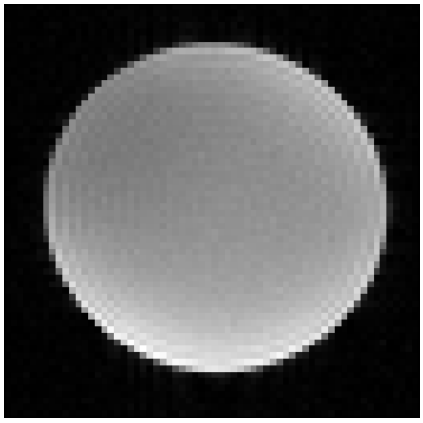

Figure 2.3: *Example of Gibbs-ringing in an agarose phantom measured in the 7T Bruker scanner. The Gibbs-ringing originates from the interface between the phantom and its surrounding area.*

There are several methods that try to remove, or at least reduce, the Gibbs-ringing artifact. One of the easiest methods to remove the oscillations is to try to smoothen out the image by applying a median filter. This method is fast and easy, but it also causes a global blurring of the image, effectively reducing spatial resolution. More sophisticated methods have been proposed and developed[15][16][17].

We have implemented the method proposed by Kellner et al.[18], which uses local subvoxel-shifts to remove (or reduce) the Gibbs-ringing artifact. This works the following way: k-space is sampled on a discrete grid, as opposed to on a continuous domain. Therefore the strength of the Gibbs-ringing is predominantly determined by the precise location of the sharp transition on the discrete sampling grid. In real space this translates to the way the sinc function is sampled. More precisely, the strength of the ringing artifact is dependent on the location of the sharp transition with respect to the sinc's sampling grid.

In Figure 2.4 (left) we see an image with a sharp transition which is reconstructed from truncated k-space data. This figure shows that the ringing artifact is strongest when sampled at the extrema of the sinc function. The right image of Figure 2.4 shows the same sharp transition, this time sampled at the zero-crossing of the sinc function, heavily suppressing the ringing artifact. Thus shifting the sinc with respect to the discrete sampling grid in such a way that the sinc's zero crossings are the points that

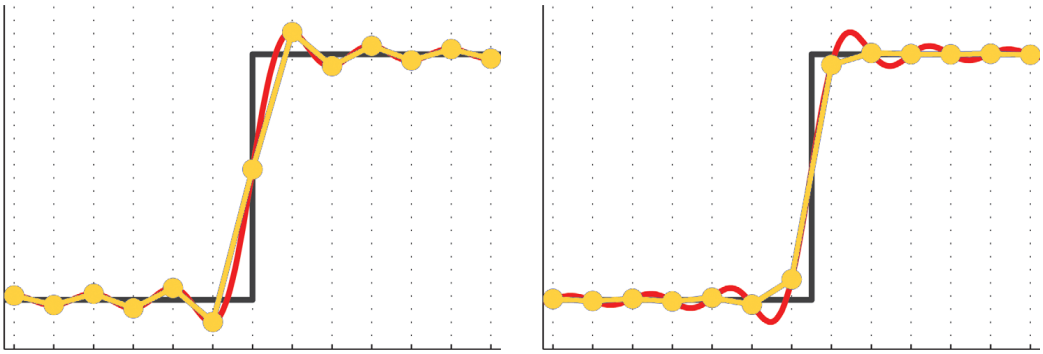

Figure 2.4: *An image with a sharp transition (black edge) which is reconstructed from truncated k-space data. Left: the resulting image (yellow interconnected dots) is sampled at the extrema of the sinc (red line) and therefore shows ringing artifacts. Right: the same image, this time sampled at the zero-crossings of the sinc. The amplitude of the ringing is significantly decreased in the image sampled at the zero-crossings of the sinc. Image adapted from Kellner[18].*

are sampled can greatly reduce the Gibbs-ringing strength. This shift is referred to as the optimal subvoxel shift. As the optimal shift for a given pixel depends on the local contrast and geometry, a global shift will not achieve a sufficient correction everywhere. The shift will need to be calculated for every pixel separately.

1D case

We start with the original reconstructed image $I_0(x)$, with Fourier coefficients $c_0(k)$. We create a set of $2M$ shifted images $I_s(x)$:

$$I_s(x) = \frac{1}{N} \sum_{k=0}^{N-1} c_0(k) e^{\frac{-2\pi i}{N} k(x + \frac{s}{2M})}, \quad s = -M, -M+1, \ldots, M-1 \tag{2.49}$$

Here the integer s defines the shift of $\frac{s}{2M}$ of image I_s.

Now, to find the optimal shift s we determine the total variation[9] in the neighborhood of every pixel. The definition of this neighborhood is very important. For example: when pixel x is located right on a sharp transition in the image, it could be useful to exclude pixel x from the total variation calculation. This is because than the total variation will not include the large transition, but only the oscillations.

Also, Kellner et al.[18] found it was beneficial to calculate the total variation on the left ($x' < x$) and right ($x' > x$) side separately. Therefore the

[9] The total variation between pixels is equal to their absolute difference.

oscillation measure $D_s^{\pm}(x)$ is calculated for the left (+) and right (-) side separately:

$$D_s^{\pm}(x) = \sum_{n=k_1}^{k_2} |I_s(x \pm n) - I_s(x \pm (n-1))| \tag{2.50}$$

where $K = [k_1, k_2]$ is the neighborhood in which the total variation is calculated. The optimal shifts $t^{\pm}(x)$ are determined separately for both sides:

$$t^{\pm}(x) = \underset{-M \leq s \leq M}{\operatorname{argmin}} D_s^{\pm}(x) \tag{2.51}$$

Now the optimal shift $t(x)$ is determined by the overall minimum:

$$t(x) = \min \left(D^+_{t^+(x)}, D^-_{t^-(x)} \right) \tag{2.52}$$

This is the $t(x)$ that minimizes the oscillations.

Since the shifts per pixel would create image distortions, we have to redistribute the shifted image onto the original pixel grid by linear interpolation[10].

2D case

We can use the 1D algorithm to reduce the Gibbs-ringing artifact in 2D images. For this we need to reduce the 2D Gibbs-ringing in a 2D image to two times a 2D image, both containing 1D Gibbs-ringing[11]. Kellner et al used a smart scheme to accomplish this.

Starting from the original image (panel a in Figure 2.5), we divide the 2D Gibbs-ringing removal into two steps: one for removal in the x direction and one for removal in the y direction.

Next we define two filter functions, G_x and G_y, which have a saddle-like structure in k-space:

[10] Any kind of back interpolation could be chosen, however linear interpolation definitely does not introduce any unwanted oscillations, which is not always the case when using higher order interpolation. Using sinc interpolation would result in the original image, including all the Gibbs-ringing oscillations we set out to remove.

[11] With 1D Gibbs-ringing in a 2D image we mean that Gibbs-ringing is only prevalent in only one of the two image directions.

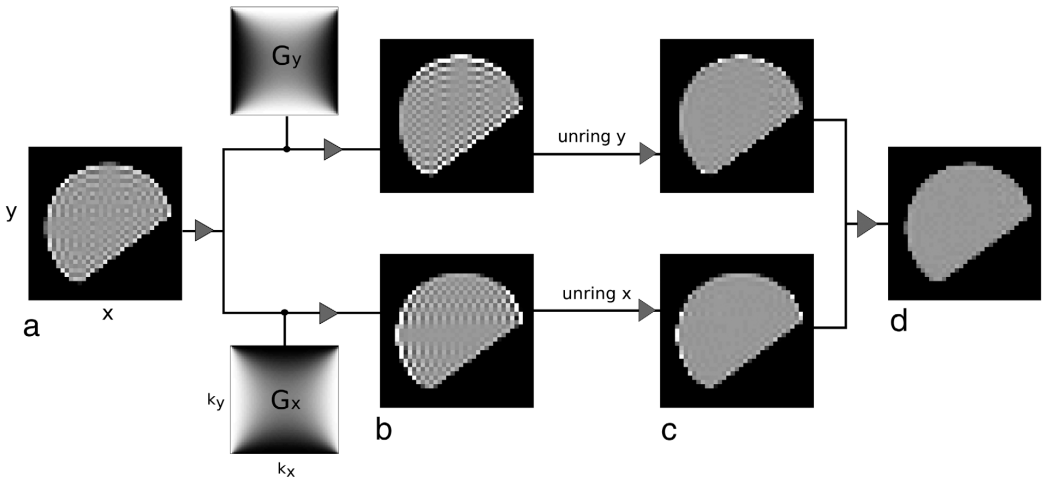

Figure 2.5: *2D Gibbs-ringing removal process. The original image (a) is convolved with the filters G_x and G_y in k-space. This procedure removes Gibbs-ringing from one direction and enhances it in the other direction (b). The 1D Gibbs-ringing removal algorithm is applied to the two images along the direction still showing heavy ringing. This reduces the Gibbs-ringing in those directions substantially (c). Finally both images are averaged to produce the final image (d). Image reproduced from Kellner[18].*

$$G_x = \frac{1 + \cos k_y}{(1 + \cos k_y) + (1 + \cos k_x)} \tag{2.53}$$

$$G_y = \frac{1 + \cos k_x}{(1 + \cos k_y) + (1 + \cos k_x)} \tag{2.54}$$

These filters will suppress high frequency oscillations in one direction and enhance them in the other direction (panel b in Figure 2.5). Also, they are normalized: $1 = G_x + G_y$. They are applied separately to the Fourier transform of the original image:

$$I_x = FT^{-1}\{FT\{I\} \cdot G_x\} \tag{2.55}$$

$$I_y = FT^{-1}\{FT\{I\} \cdot G_y\} \tag{2.56}$$

Now the 1D algorithm is applied to I_x in the x direction and to I_y in the y direction (panel c in Figure 2.5). These images are then averaged to produce the final 2D image with reduced Gibbs-ringing (panel d in Figure 2.5). The normalization of the filters G_x and G_y assures that we have not introduced any smoothening in the image.

In the case of a 3D image, we apply the 2D Gibbs-ringing algorithm to each slice separately.

Proof of Principle

We tested the 2D Gibbs-ringing artifact removal algorithm by taking an image and inducing Gibbs-ringing into it. Gibbs-ringing can be induced in an image by taking its Fourier transform, cutting a piece of k-space off and then Fourier transforming back to real space. The amount of k-space cut off influences the frequency of the induced Gibbs-ringing in the image.

We did this twice, one for a lower frequency (left image in Figure 2.6) and one for a higher frequency (left image in Figure 2.7). Next we applied the 2D Gibbs-ringing removal algorithm to the images. The neighborhood K that we used consists of 3 neighboring points excluding the point on which the correction is applied.

The results for the low frequency ringing are presented in the right image of Figure 2.6, while the results for the high frequency ringing are presented in the right image of Figure 2.7. In both images, many of the oscillations have been suppressed. However, in the higher frequency Gibbs-ringing image, higher order oscillations are still visible after correction. To the contrary, in the lower frequency Gibbs-ringing image almost all higher order oscillations are suppressed. This indicates that the algorithm works better when the frequency of the ringing is lower, which is to be expected. This is due to the fact that the algorithm is based on minimizing the local total variation and the local total variation of an image with a higher frequency oscillation is inherently larger.

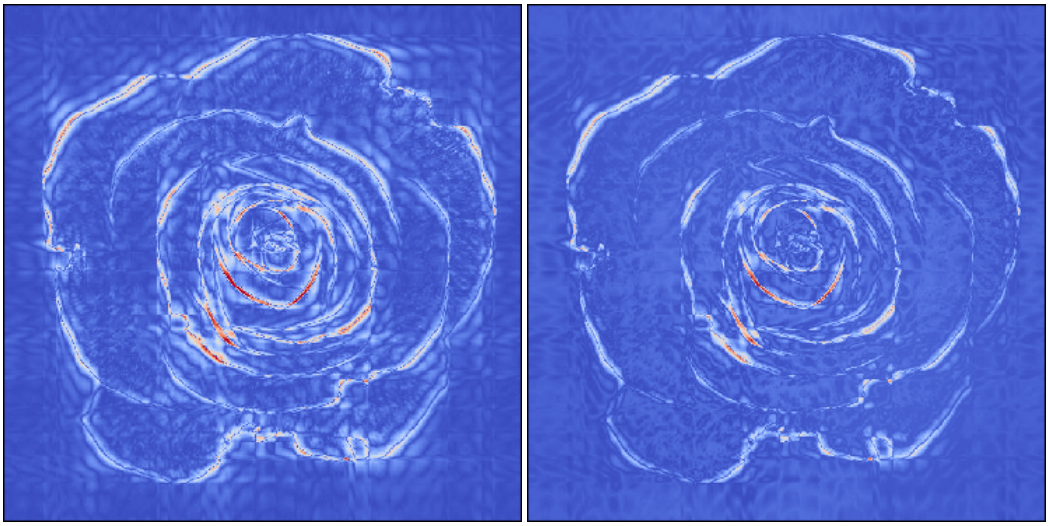

Figure 2.6: *Low frequency Gibbs-ringing test. Left: original image of a rose with induced low frequency Gibbs-ringing. Right: left image after Gibbs-ringing correction. Many of the oscillations have been removed, or at least reduced. Almost all higher order oscillations have been removed.*

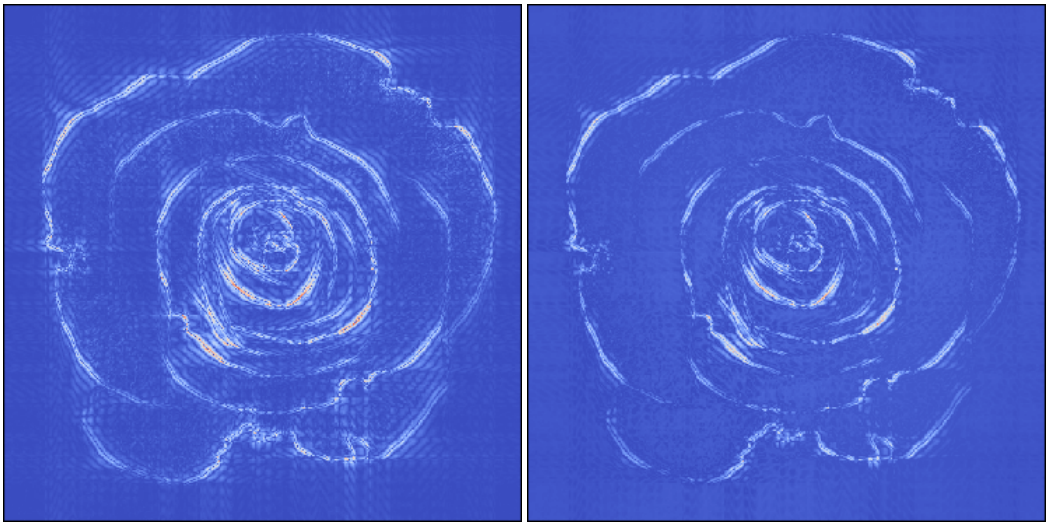

Figure 2.7: *High frequency Gibbs-ringing test. Left: original image of a rose with induced high frequency Gibbs-ringing. Right: left image after Gibbs-ringing correction. Many of the oscillations have been removed, or at least reduced. Some of the higher order oscillations are still visible in the image.*

Chapter 3

Methodology

In this chapter we present the samples that we produced to mimic the human cortex. Also, we introduce the MRI protocols used for mapping the B_1^+ phase. To close off this chapter, we describe the Python pipeline that we created, which handles all post-processing necessary for reconstructing conductivity maps.

3.1 Phantoms

We have selected agarose, an organic polysaccharide, to mimic the human brain. Agarose shares a lot of properties with grey matter in the brain. Most importantly they have comparable proton densities and an approximately equal T_2 time of 80ms[7][19].

Agarose is commercially available as a white powder. It can be dissolved in near-boiling water, a temperature of 85°C or higher is sufficient. When it cools down, it forms a gel[1].

The gel's electrical properties are dependent on additives that are dissolved in the water together with the agarose powder. The conductivity of the gel can be influenced by adding sodium chloride and regular sugar. For low conductivities ($\sigma \leq 2\frac{\mathrm{S}}{\mathrm{m}}$) the concentration of sodium chloride predominantly determines the conductivity. Only for large conductivities the concentration of sugar starts to influence the conductivity[20]. The ratio[2]

[1] Agarose exhibits thermal hysteresis in the liquid-gel transition. It liquefies and jellifies at different temperatures.

[2] The exact ratios of salt and sugar necessary for specific conductivities and permittivities can be found here: https://amri.ninds.nih.gov/cgi-bin/phantomrecipe.

of salt and sugar will determine the conductivity and permittivity of the final agarose gel.

Of course adding magnetite to the solution will influence the conductivity as well. In 2017 Nurdin[5] reported electric conductivity enhancements of maghemite (Fe_2O_3) nanofluids. He found that the conductivity of the solution has a linear dependence on the maghemite concentration. However, this was for concentrations ten thousand times higher than the concentrations we use throughout the project. Also, even though maghemite is similar to magnetite (Fe_3O_4), magnetite will influence the conductivity of a solution differently.

Throughout the project we have used different sizes and shapes of agarose samples, some with and some without added magnetite. They all follow the same basic recipe. Only the salt and magnetite concentrations may differ per sample.

Agarose sample recipe

- Prepare a water bath at 85ºC. Close it with aluminum foil to prevent it from cooling down fast. This bath will be used to keep the agarose solution warm enough to stop it from jellifying.

- Prepare 200mL of milli-Q water in a flask and add 3.0g of agarose powder to create a 1.5% agarose solution. Add sodium chloride if desired. For example: a sample with a conductivity of $0.6\frac{\mathrm{S}}{\mathrm{m}}$ requires about 0.3g of sodium chloride per 100mL water.

- Microwave the flask containing the agarose solution until it reaches a temperature high enough to completely dissolve the agarose and the solution becomes transparent. Store it in the hot water bath to prevent jellifying.

- Distribute the agarose solution over the samples. If desired, add any magnetite solution to the agarose solution while it is still hot.

All products were purchased from Sigma Aldrich[3]. We used 20nm magnetite nanoparticles (LOT number: MKBX1105V), agarose (LOT number: ES521B027290) and NaCl.

[3]Sigma Aldrich Chemie B.V., Zwijndrecht.

3.2 MRI Protocols

In this section we briefly describe the MRI protocol used during image acquisition. We use a very basic spin echo sequence, as presented in Figure 3.1.

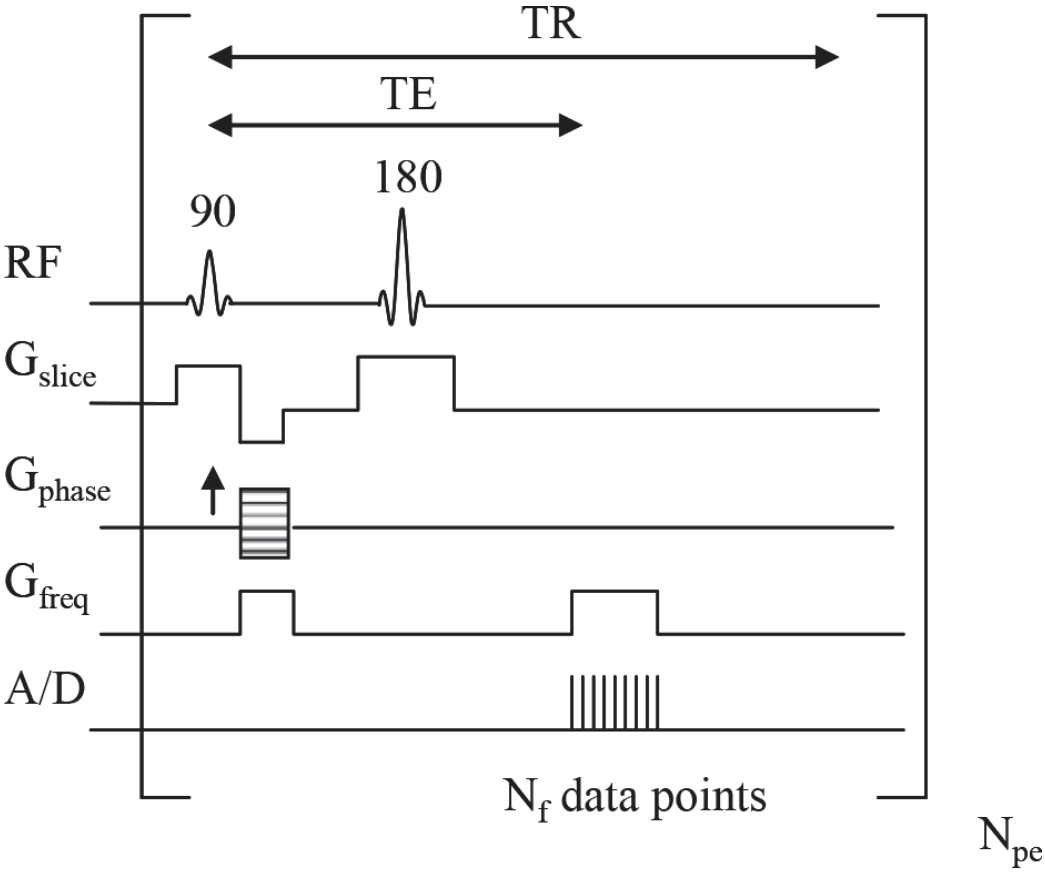

Figure 3.1: *Basic spin echo sequence used for image acquisition. See main text for explanation. Image reproduced from Smith & Webb[21].*

The first step is to apply a 90º RF pulse to the sample. There are three different gradients (G_{slice}, G_{phase} and G_{freq}) applied at different times, for spatial encoding of the sample[4]. After a time $\frac{TE}{2}$ has passed, a second RF pulse of 180º is applied. Due to this pulse, the extrinsic field inhomogeneities cancel out, leading to a partial spin refocusing at a time TE, giving rise to the so-called 'spin echo'. During this echo data points are sampled.

[4]For an excellent coverage on how gradients are used to identify spatial postion, see Smith & Webb[21].

To sample the volume of the sample faster, instead of doing the spin echo sequence per slice, we used a Multi-Slice Multi-Echo (MSME) sequence, which can be used to acquire many adjacent slices during one TR interval. We adapted this sequence so that we are able to use its Multi-Slice part, with only a single echo.

As mentioned in Section 2.3, we repeated this acquisition with all read-out gradients inverted (see Figure 3.2 for details), to cancel out the eddy current contribution to the measured phase.

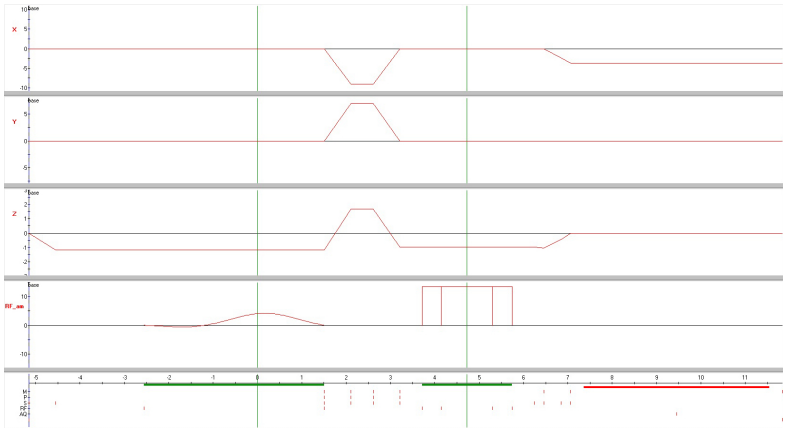

(a)

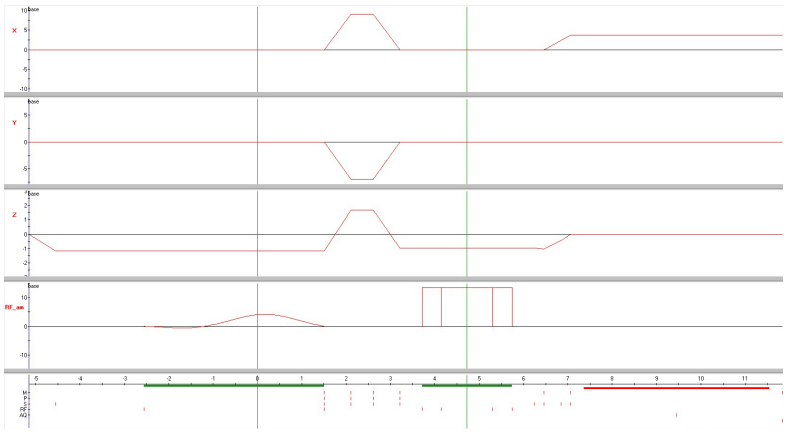

(b)

Figure 3.2: *(a): Gradient and pulse diagram for the MSME sequence. (b): Same diagram with the sign of the read-out gradients inverted.*

3.3 Python Pipeline

For all post-processing of the MRI images we use a home-written Python 2.7 script. A schematic of the full process is depicted in Figure 3.4.

First we import the MRI images (phase and magnitude) and all metadata. Since we have used three different MRI scanners from two brands that both use different file formats, we have to either import DICOM files (Philips scanners) or multiple files (2dseq and parameter files) belonging to the ParaVision file structure (Bruker scanner). We import, rescale[5], and sort every slice included. Also all scan parameters necessary for the computation are imported[6].

Next we require the user to input their preferred reconstruction settings. The first option is to apply a 3D phase unwrapping algorithm on the images. Sometimes a phase wrap, a spot where the jump from one pixel to another is 2π, is present in the phase image. For the normal conductivity reconstruction using Equation 2.43 phase wraps would not affect the results, since an extra factor of 2π in a complex exponent is arbitrary. However, for the Gibbs-ringing removal algorithm presented in Section 2.5 it is a problem. This algorithm uses total variation calculations to find the optimal local subvoxel shift that minimizes Gibbs-ringing. A sudden phase jump of 2π will interfere with minimizing the total variation. Therefore, whenever phase wraps are present in the images, an unwrapping algorithm will need to be used before Gibbs-ringing correction can be applied. For the unwrapping we use the method developed by Herráez et al.[22], a result of which is presented in Figure 3.3. Their algorithm changes the phase values by integer values of 2π smartly, removing the phase wrap.

The next option is whether to apply Gibbs-ringing correction or not. This correction is performed slice by slice, so 2D.

The last option is to chose which kernel is used for the calculation of the numerical Laplacian (see Section 2.4). Each Laplacian is calculated by convolving the chosen kernel with the 2D (or 3D) array containing the complex exponent of the phase image (see Equation 2.43 for details).

Before any post-processing of the images begins, three different masks[7]

[5] All MRI images are stored as 16 bit unsigned integers in binary format. Of course phase maps with a range from $-\pi$ to π cannot be accurately stored in this file format. Therefore, for every slice there is a linear conversion factor that rescales the 16 bit unsigned integers to 16 bit floating point numbers in the correct range.

[6] The most important parameters are scan resolution (x, y and z), Larmor frequency (or field strength), slice rescale factors and image orientation.

[7] Masks are used to exclude certain pixels from calculations. For example for the phase unwrapping method it is essential to exclude most of the pixels not lying in a sample.

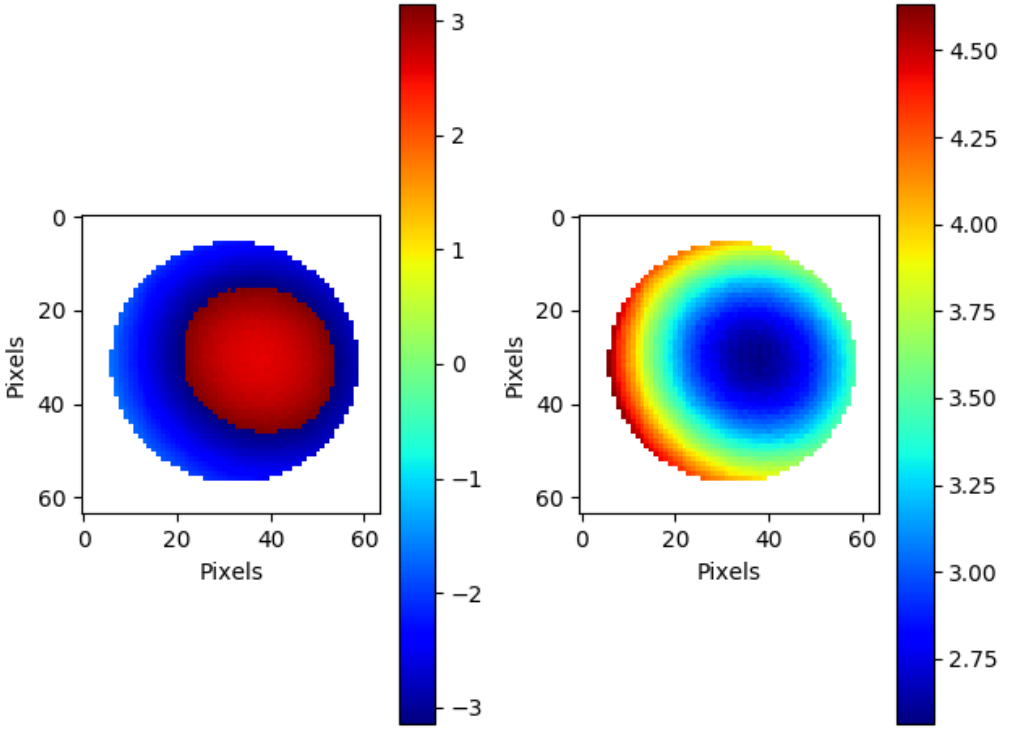

Figure 3.3: *Left: masked phase image of an agarose tube acquired with the Bruker 7T scanner. The resolution is 0.5mm in both directions. In the middle of the tube we see a phase wrap, where the jump from one pixel to another is 2π. Right: same phase image, unwrapped using the algorithm by Herráez et al.[22].*

are calculated for every slice. Here we assume that there might be multiple samples in the maps and they are all circularly shaped[8].

The first mask contains all samples with their correct size. This mask is used for calculating and plotting the conductivity reconstruction.

The second and final mask contain the same regions, only with a smaller and larger radius. These latter masks are used to exclude the boundaries of the circular samples in calculations like SNR (Signal to Noise Ratio) and the average and standard deviation of all pixels inside the sample. For the SNR this method of calculation is standard. For the mean and standard deviation of the conductivity of all pixels included in the sample it is imperative to exclude the boundaries in the calculation. In Section 2.3 we saw that, for the reconstruction using the B_1^+ phase only, we need the variation

[8]Only small modifications need to be made to the script if other shapes of samples are used.

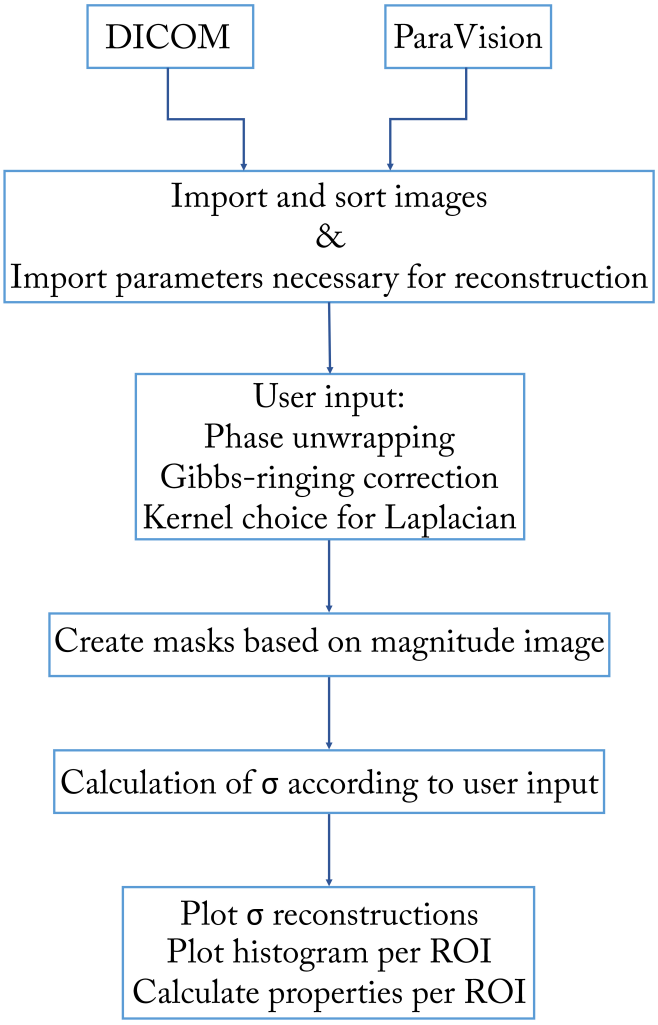

Figure 3.4: *Python pipeline diagram. See main text for details.*

in the magnitude of the B_1^+ field to be sufficiently small. At the boundaries of the samples this is not the case, so the boundaries need to be excluded from the calculation. Moreover, when using the kernels that include a smoothening operation ($k_{2D-large}$ and k_{3D}) to calculate the Laplacian (see section 2.4), the boundary error propagates further into the sample. The maximum number of pixels included in the smoothening operation is 7. Therefore the smallest mask will contain regions with a radius of 7 pixels smaller compared to the mask containing the actual sample's dimensions. The opposite holds for the largest mask.

In Figure 3.5 we show the conductivity reconstruction pipeline. We start by importing both the phase image (**a**) measured with standard read-

out gradients as well as the phase image (**b**) measured with inverted readout gradients. We also import the magnitude image (**c**) and create a mask based on this image (**d**). Using Equation 2.47 we calculate the transmit phase ϕ_+ (**e**). Lastly, we calculate the conductivity map (**f**) using Equation 2.43 and create a histogram based on all points present within the smallest mask.

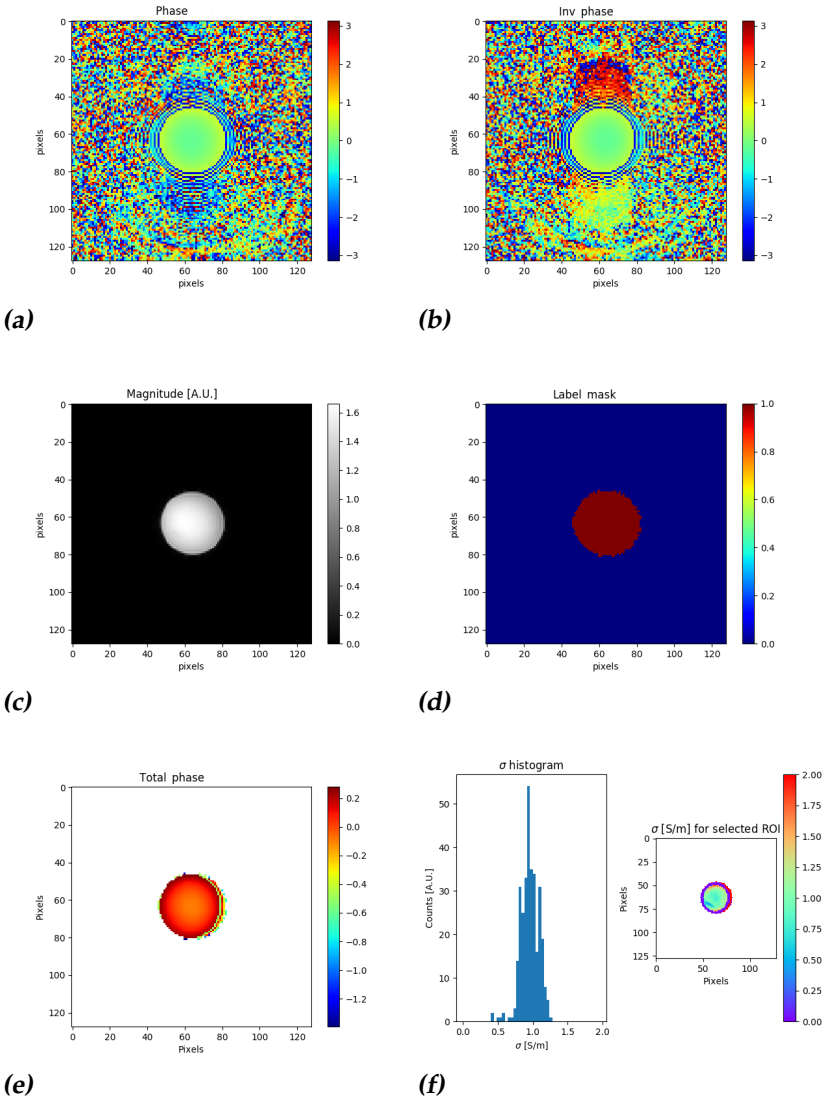

Figure 3.5: *Conductivity reconstruction pipeline. (a): Phase image of a sample containing agarose and NaCl, acquired with a 7T Philips MRI scanner. (b): Phase image acquired with the sign of the read-out gradients inverted. (c): Magnitude image. (d): Mask based on magnitude image. (e): Masked image of the transmit phase obtained by combining (a) and (b), see Section 2.3 for details. (f): Masked conductivity reconstruction and histogram using the* $k_{2D-large}$ *kernel.*

Chapter 4

Results & Discussion

In this chapter we present conductivity reconstructions of samples consisting of agarose and NaCl as well as samples with added magnetite. Additionally, we compare the performance of the three different kernels that can be used for the reconstruction.

4.1 Kernel Comparison & NaCl Conductivity Reconstructions

Throughout this project we have used three MRI scanners: the 7T Bruker scanner, the 7T Philips scanner and the 3T Philips scanner. We will specify which was used for every measurement. Unless specified otherwise, we used a repetition time (TR) of 800ms and an echo time (TE) of 9ms for the measurements.

In Figure 4.2, 4.3 and 4.4 we present a performance comparison between the three kernels: $k_{2D-small}$, $k_{2D-large}$ and k_{3D}. For the comparison we measured eight slices of a single tube containing agarose and NaCl. We aimed for a conductivity of $1\frac{\mathrm{S}}{\mathrm{m}}$ at 300MHz[1] of the agarose gel. We measured[2] an ac conductivity of $0.935\frac{\mathrm{S}}{\mathrm{m}}$ at 300MHz. The 7T Philips scanner was used for this measurement and the phase maps were averaged twice.

Slices 1 and 8 are the ends of the agarose in the tube, explaining the low conductivity of the bulk material in these slices. Slices 2 to 7 contain the bulk of the agarose sample. Generally the reconstructions us-

[1] 300MHz is the Larmor frequency for protons at 7T.

[2] We measured the ac conductivity of the sample using a dielectric assessment kit (DAK-12, SPEAG, Zürich, Switzerland) and a network analyzer (TR1300, CMT, Indianapolis, USA).

ing the $k_{2D-small}$ kernel are noisy compared to the reconstructions using the other kernels. This is to be expected, since the other kernels apply a smoothening operation to the σ map, while $k_{2D-small}$ does not. Moreover, noise is amplified when calculating derivatives. Consequently, without a smoothening operation the σ maps will be inherently noisy. Increasing the number of averages will reduce the noise in the phase maps, thereby also reducing the noise in the σ maps. However, this can be very time consuming and therefore unpractical.

Slice	$\bar{\sigma}$ k_{2D-s}	SD k_{2D-s}	$\bar{\sigma}$ k_{2D-l}	SD k_{2D-l}	$\bar{\sigma}$ k_{3D}	SD k_{3D}	SNR
1	0.145	0.664	0.176	0.244	0.271	0.128	1306
2	0.769	0.544	0.779	0.151	0.691	0.146	1421
3	0.923	0.512	0.939	0.124	0.908	0.117	1455
4	0.969	0.572	0.973	0.129	0.957	0.131	1504
5	0.894	0.719	0.914	0.264	0.910	0.207	1532
6	0.817	0.741	0.832	0.295	0.819	0.251	1503
7	0.672	0.818	0.669	0.211	0.638	0.227	1462
8	0.402	1.585	0.394	0.338	0.360	0.211	1380

Table 4.1: *Mean conductivity values ($\bar{\sigma}$) and standard deviation (SD) for the conductivity reconstructions presented in Figure 4.2, 4.3 and 4.4. SNR values are determined from the magnitude maps of the slices.*

In Table 4.1 we show the mean and standard deviation of all slices in Figure 4.2, 4.3 and 4.4. In slices 3 to 5, using $k_{2D-large}$ and k_{3D}, we recover the mean conductivity of the sample: $0.935\frac{\mathrm{S}}{\mathrm{m}}$. The noisiness of all reconstructions processed with the $k_{2D-small}$ kernel can be inferred from the standard deviation: the standard deviation is large when compared to the other kernels. The $k_{2D-large}$ and k_{3D} kernels perform equally well: the standard deviation is low.

The mean conductivity values of slices 2, 6 and 7 generally show a lower $\bar{\sigma}$ and larger standard deviation. We always place the sample at the isocenter of the MRI scanner, meaning the B_0 field is the most homogeneous in the middle of the sample (slices 3-5). That is also where the SNR is maximized, as is also clear in Table 4.1. Outside of the isocenter we see the SNR decrease and consequently also the conductivity reconstruction starts to fail. Therefore, a high SNR is imperative for a correct conductivity reconstruction.

All reconstructions show boundary error propagation in the sample. This error is due to one of the constraints mentioned in Section 2.3: the variation in the magnitude of the B_1^+ field should be sufficiently small com-

pared to the variation in its phase. In the bulk of the sample this requirement is met, but at the boundary between sample and air it no longer holds. We exclude the boundary errors from the statistical analysis.

The error is more severe for the slices processed using the kernels including a smoothening operation. Since these kernels smoothen over 7 pixels in-plane (xy) the boundary error propagates farther into the sample then that it would due to a normal three-point derivative. Including the B_1^+ magnitude in the calculation might correct the boundary error.

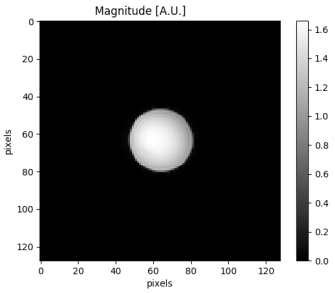

Figure 4.1: *Magnitude image of slice 4 in Figure 4.2, 4.3 and 4.4.*

To summarize: when the SNR is sufficient, we are able to reliably reconstruct the bulk of the conductivity map up to $\pm 0.2 \frac{\mathrm{S}}{\mathrm{m}}$. The SNR is maximized at the isocenter of the MRI scanner. Whenever the SNR is too low the reconstruction deteriorates. Likewise, due to the boundary error propagation, the reconstruction typically shows large errors at the boundaries of the sample.

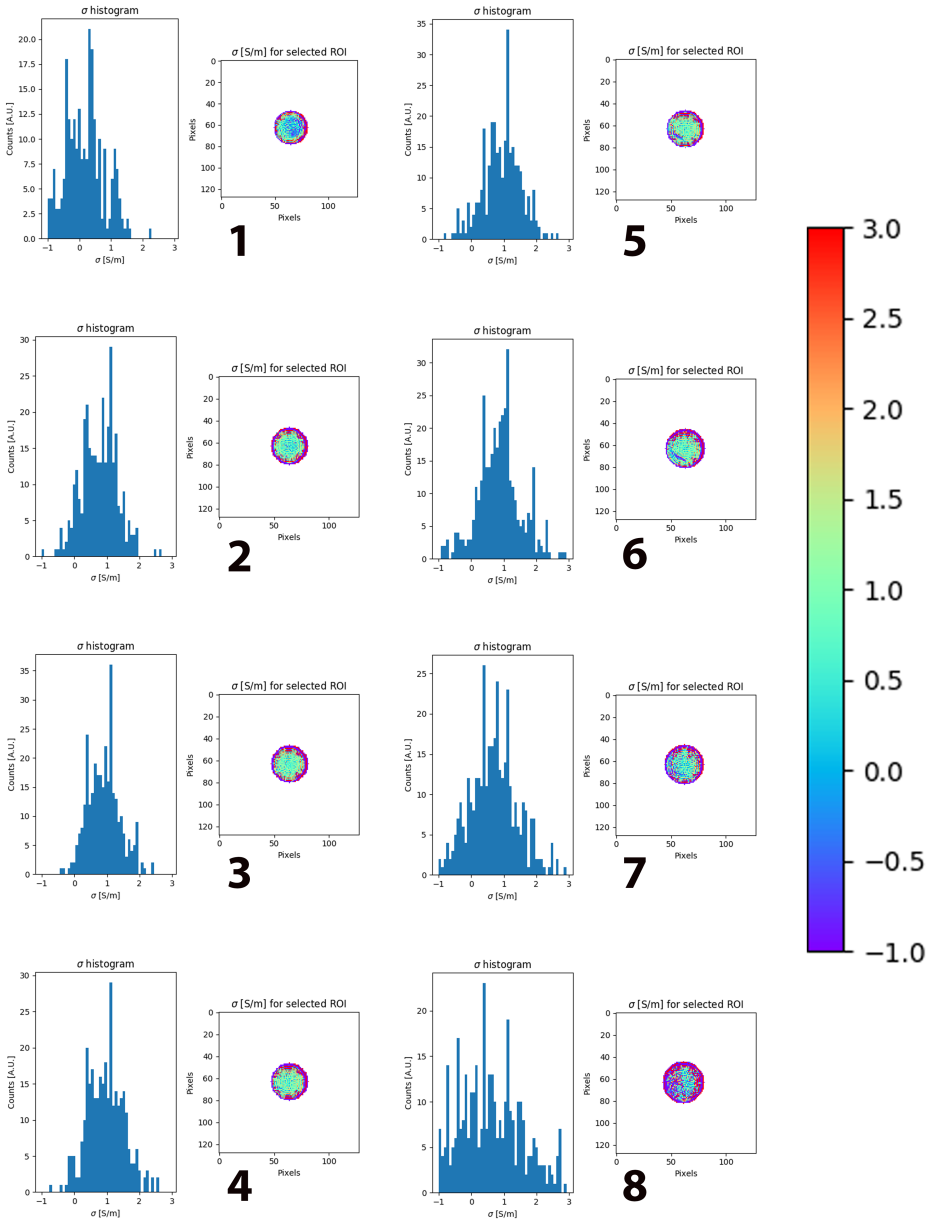

Figure 4.2: *Conductivity reconstructions of eight different slices acquired with the 7T Philips scanner. The sample is a single tube filled with agarose and NaCl and for the reconstruction we used the $k_{2D-small}$ kernel. The resolution is 1.51$\frac{mm}{pixel}$ in both directions. The first image is the top of the tube, the last image is the bottom. In slices 3-5 we recover the sample's conductivity of 0.935$\frac{S}{m}$. However, the reconstructions are noisy. This is also clearly visible in the histograms: the spread is significant. Slices 1 and 8 are the ends of the tube, explaining the bad reconstruction.*

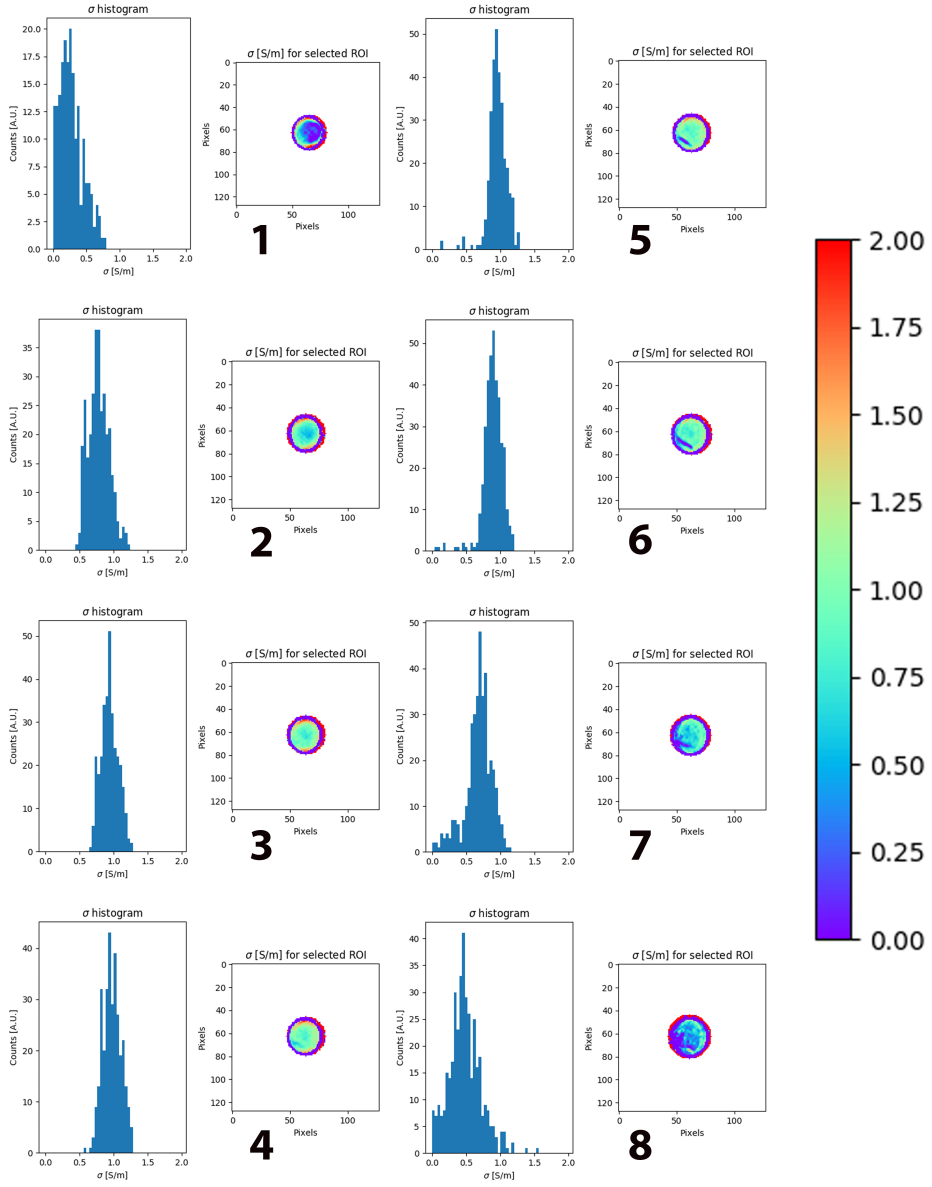

Figure 4.3: *Same data as in Figure 4.2, here reconstructed using the $k_{2D-large}$ kernel. Again, in slices 3-5 we recover the sample's conductivity of 0.935$\frac{S}{m}$. This time the reconstructions are less noisy. This result is confirmed by the histograms, in which the spread is significantly reduced. Slices 1 and 8 are the ends of the tube, explaining the bad reconstruction.*

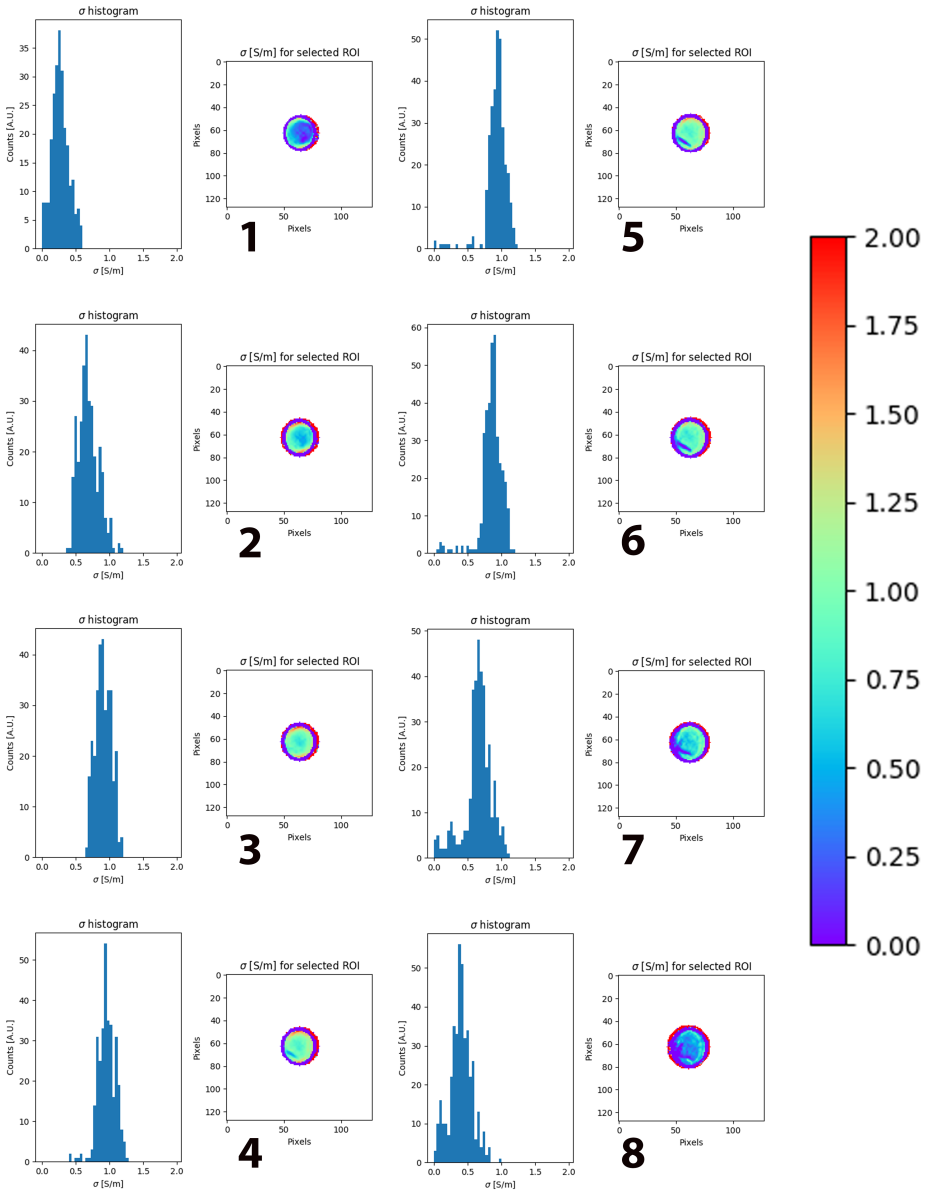

Figure 4.4: *Same data as in Figure 4.2, here reconstructed using the k_{3D} kernel. Again, in slices 3-5 we recover the sample's conductivity of $0.935\frac{S}{m}$. Here we see similar results as in Figure 4.3: the reconstructions are less noisy and the spread in the histograms is small.*

4.2 Magnetite Conductivity Reconstructions

The goal of this project is to test if the EPT method can be used to differentiate a sample mimicking a healthy brain's grey matter from another containing magnetite nanoparticles in a concentration similar to that found in the brain cortex of Alzheimer's disease patients. The concentration of iron in the brain of Alzheimer's patients is roughly 1mM in the frontal cortex[7][8].

We produced a sample consisting of two sections: one containing agarose and NaCl (we aimed for a conductivity of $0.6\frac{\mathrm{S}}{\mathrm{m}}$), the other containing the same with added magnetite nanoparticles in a concentration of $35\frac{\mu\mathrm{g}}{\mathrm{mL}}$, leading to an iron concentration of 0.45mM. This is an iron[3] concentration comparable to what is found in the frontal cortex. We measured 32 slices of this sample with the 3T and 7T Philips scanners, 16 of which are of the magnetite-doped part of the sample.

In Figure 4.5 we present the conductivity reconstructions of four slices of the sample described above. Panels (a) and (c) contain a slice with only agarose and NaCl, panels (b) and (d) contain a slice with added magnetite. Panels (a) and (b) were measured using the 3T Philips scanner, (c) and (d) were measured using the 7T Philips scanner.

Both reconstructions of the 3T scanner are remarkably similar. Only the boundary effect has switched sign for a part of the reconstruction of the magnetite slice. However, since we completely exclude the boundaries for all calculations, this will not affect the histograms. The reconstructions are noisy, even though they have been processed using the $k_{2D-large}$ kernel.

The reconstructions of the 7T scanner are a lot less noisy. The spread in the histograms is lower and consequently also the standard deviation is lower. The SNR in the slices measured with the 7T Philips scanner is significantly larger than the SNR in the slices measured with the 3T Philips scanner, which explains the decrease in standard deviation.

The difference between the reconstructions with and without magnetite is an increase in standard deviation for the magnetite-doped slices. This might be due to potential aggregation of magnetite nanoparticles, locally influencing conductivity. Additionally, we see a general SNR difference between the slices with and without magnetite. From the average conductivity we cannot indicate a clear difference between the two sets of slices (see panel (a) in Figure 4.6). Therefore, the current reconstructions are not sensitive enough to conclusively detect conductivity changes due to the

[3]This iron concentration is comparable to what is found in the frontal cortex. However, not all of the iron in the brain is due to magnetite.

concentration of magnetite found in the brain.

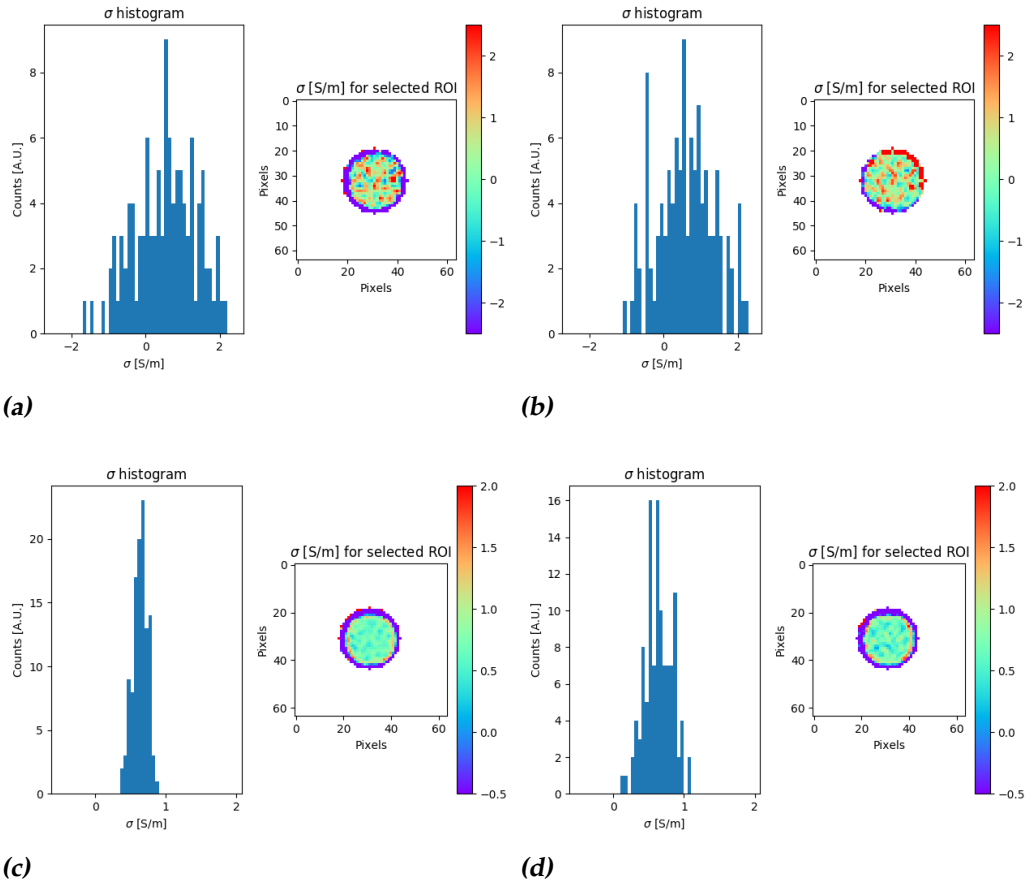

Figure 4.5: *Conductivity reconstructions of four different slices. The slices in panels (a) and (b) were measured with the 3T Philips scanner, the others with the 7T Philips scanner. The resolution is* $1\frac{mm}{pixel}$ *in both directions and the* $k_{2D-large}$ *kernel was used for processing. (a), (c): Reconstruction of a slice of a sample containing agarose and NaCl. (b), (d): Reconstruction of a slice of a sample containing agarose, NaCl and magnetite (magnetite concentration:* $35\frac{\mu g}{mL}$*).*

Now let us investigate why the sensitivity of the reconstructions is too low to detect conductivity changes due to magnetite. In 2018, Radoń et al.[23] found that the ac conductivity of 10nm magnetite nanoparticles is (after extrapolation) approximately $8 * 10^{-2}\frac{\mathrm{S}}{\mathrm{m}}$ at 300MHz. To calculate the conductivity of a mixture of magnetite nanoparticles and agarose gel, we can use the model proposed by Bagheli et al.[24]. To simplify the calculation we assume that conductivity due to Brownian motion and exposure

to an electric field is negligible compared to the conductivity described by the Maxwell model. The Maxwell model is based on a static analysis of diluted and randomly distributed, non-interacting spherical components included in a homogeneous medium.

Under these assumptions the conductivity of the solution is given by:

$$\frac{\sigma_{Total}}{\sigma_{Solvent}} = 1 + \frac{3(\alpha - 1)\Phi}{(2 + \alpha) - (\alpha - 1)\Phi} \tag{4.1}$$

where σ_{Total} denotes the conductivity of the solution, $\sigma_{Solvent}$ the conductivity of the agarose gel, $\alpha = \frac{\sigma_{Magnetite}}{\sigma Solvent}$ and Φ is the particle volume fraction.

The conductivity of the solvent, in this case agarose, is $0.6\frac{\mathrm{S}}{\mathrm{m}}$. Therefore we find a value for α of 0.02. The particle volume fraction (Φ) of magnetite in the sample is $6.8 * 10^{-6}$. Using these values in Equation 4.1 we find a conductivity change of approximately $10.25 * 10^{-6}\frac{\mathrm{S}}{\mathrm{m}}$.

Keep in mind that this is a 'worse case' estimate. We neglected the contributions of both the Brownian motion and particle movement due to exposure to electric fields. Moreover, the ac conductivity of 20nm magnetite nanoparticles could be different than the conductivity of 10nm nanoparticles. However, even though it is a 'worst case' estimate, this analysis indicates that the sensitivity of the reconstructions will need to be significantly improved before it will be able to detect changes in the mean of the conductivity reconstruction due to low concentrations of magnetite.

The largest improvement of the sensitivity of the reconstruction can be achieved by improving the acquisition of the phase maps. We have seen that the images with the highest SNR result in the most accurate reconstructions. Moreover, the resolution of the phase maps plays an important role in the smoothness of the reconstruction. Calculation of the Laplacian with the kernels including a smoothening operation improves the smoothness significantly. However, filtering an image might also alter some of the details and structure in the image.

Since increasing the resolution will automatically reduce the SNR, improving SNR and resolution together will not be easy. From Table 4.1 we see that only a small dip in SNR results in an incorrect reconstruction. Therefore, improving the SNR is more important and can be done simply by taking more averages. However, this comes at the expense of a much longer scan time.

We have been unable to measure a difference in the mean of the conductivity. However, we have been able to observe a difference in standard deviation. In panel (b) of Figure 4.6 we present the standard deviation of every slice. All slices with a slice number lower than 17 contain no mag-

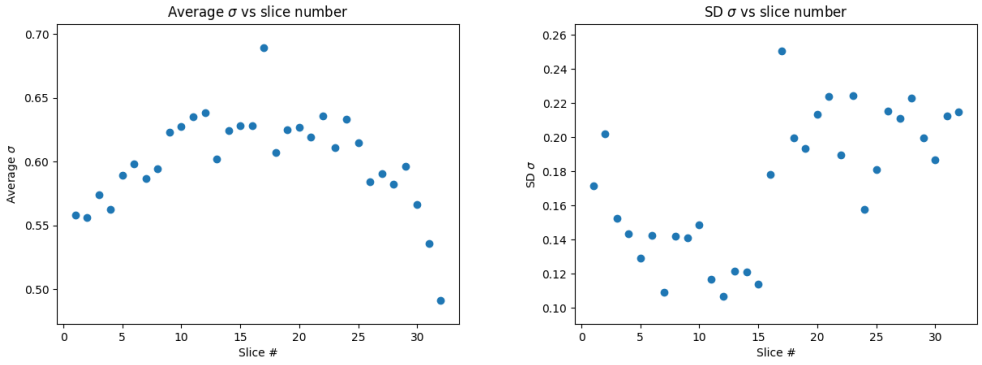

(a) ***(b)***

Figure 4.6: *(a): Average conductivity vs slice number. (b): Standard deviation (SD) vs slice number. All slice numbers lower than 17 contain no magnetite. There is less variation in the average and standard deviation when compared to the results in Table 4.1. This is because the images used for this reconstruction were averaged 80 times, keeping the variation in the SNR relatively small throughout the image volume. Only for the first and last 5 slices the reconstruction starts to be negatively influenced by SNR.*

netite.

Here we see a clear difference: the standard deviation of slices without magnetite is about 50% lower than the standard deviation of magnetite-doped slices. This increase in standard deviation might be explained by the fact that magnetite nanoparticles tend to aggregate, locally influencing the conductivity more due to the higher local concentration. Since the variation of the SNR is small throughout the image volume, the increase in standard deviation is not directly related to a decrease in SNR.

A more extensive analysis should be done before any conclusions can be drawn from this observation.

Chapter 5

Conclusion

At the start of this thesis we set out to test if the EPT method can be used to detect conductivity changes due to magnetite concentrations found in the human brain. We did this to find out if a change in tissue conductivity due to the presence of magnetite might be a viable biomarker for diagnosing Alzheimer's disease.

We presented the theory on which the conductivity reconstruction is based: the homogeneous Helmholtz equation. To this we added the B_1^+ phase-only approximation, which, under certain constraints, allows simpler calculations than the full Helmholtz equation. We introduced three different kernels to calculate the Laplacian occurring in the calculation for the conductivity reconstructions. Two of which include a smoothening operation to prevent noise amplification during calculation.

We produced phantoms to mimic the human brain. They consist of agarose gel, a substance possessing similar properties as grey brain matter in the human brain. NaCl and magnetite nanoparticles were added to influence the conductivity of the phantoms.

Two MSME sequences were used for the acquisition of the B_1^+ phase maps: one with standard and one with inverted read-out gradients. A combination of these phase maps was used to retrieve the transmit phase map.

For all the post-processing a Python 2.7 script was written. This script can be used to unwrap the phase, reduce Gibbs-ringing and calculate conductivity reconstructions using either 2D or 3D kernels. All of this can be done using either a 2D or a 3D image volume.

Now, the answer to the question which was asked already in the subtitle of this thesis, can be answered. Can we detect conductivity changes in magnetite-doped brain phantoms? The answer is: not currently. The

sensitivity is too low. Currently we can only accurately measure the conductivity of a phantom up to $0.2\frac{\mathrm{S}}{\mathrm{m}}$, which is several orders of magnitude higher than what is required to detect changes in the average conductivity due to magnetite in the concentrations found in the human brain. Nevertheless, we have promising indications that we have been able to observe a change in standard deviation of the conductivity due to the presence of magnetite.

We have provided a proof of concept as well as pinpointed the areas that need improvement. The SNR of the acquired images plays a crucial role in the reconstruction. Improvement of the SNR should therefore be the main focus point.

Additionally, a high resolution is beneficial for the reconstruction. Nevertheless, improving SNR should be prioritized over improving resolution. Also, adding the B_1^+ magnitude map in the calculation might reduce the boundary artifact occurring in the reconstructions.

Acknowledgments

To close off this thesis I would like to show my gratitude to everybody supporting me throughout the project. I would like to thank the LUMC for allowing me to work on this project. Also I would like to thank Prof.dr.ir. T.H. Oosterkamp for taking the time to be the second reader of this thesis.

Most of all, I would like to express my sincere gratitude to Dr. Lucia Bossoni and Dr. Wyger Brink for their excellent supervision, continuous support, patience and bright minds. Thank you.

Bibliography

[1] World Health Organization. http://www.who.int/news-room/fact-sheets/detail/dementia, December 2017.

[2] L. Goodman. Alzheimer's disease, a clinico-pathologic analysis of twenty-three cases with a theory on pathogenesis. *The Journal of Nervous and Mental Disease*, 117(2):97–130, 1953.

[3] D. C. Jiles. *Introduction to Magnetism and Magnetic Materials*.

[4] M. Bulk. Quantitative comparison of different iron forms in the temporal cortex of alzheimer patients and control subjects. *Scientific Reports*, 8(1), 2018.

[5] I. Nurdin. Investigation on Electrical Conductivity Enhancement of Water Based Maghemite ($\gamma - Fe_2O_3$) Nanofluids. *International Journal of Materials Science and Applications*, 6(1):32–36, 2017.

[6] Q. Pankhurst. Increased levels of magnetic iron compounds in alzheimer's disease. *Journal of Alzheimer's Disease*, 13, 2008.

[7] S. Delangre. Bottom-up study of the MRI positive contrast created by the Off-Resonance Saturation sequences. *Magnetic Resonance in Medicine*, 254:98–109, 2015.

[8] A. B. Maher. Magnetite pollution nanoparticles in the human brain. *Proceedings of the National Academy of Sciences*, 113(39), 2016.

[9] P. Zeeman. Ueber einen einfluss der magnetisirung auf die natur des von einer substanz emittierten lichtes. *Verhandlungen der Physikalischen Gesellschaft zu Berlin*, 1882.

[10] Z. Ning Chen. *Handbook of Antenna Technologies*.

[11] D. I. Hould. The principle of reciprocity in signal strength calculations, a mathematical guide. *Concepts in Magnetic Resonance*, 12(4):173–187, 2000.

[12] L. H. M. W. van Lier. B_1^+ Phase Mapping at 7T and its Application for In Vivo Electrical Conductivity Mapping. *Magnetic Resonance in Medicine*, 67(2):552–561, 2012.

[13] M. Bernstein. *Handbook of MRI Pulse Sequences*.

[14] P. Holoborodko. Smooth noise robust differentiators. http://www.holoborodko.com/pavel/numerical-methods/numerical-derivative/ smooth-low-noise-differentiators/.

[15] D. Gottlieb and C. Shu. On the gibbs phenomenon and its resolution. *SIAM Review*, 39(4):644–668, 1997.

[16] K. T. Block. Suppression of mri truncation artifacts using total variation constrained data extrapolation. *International Journal of Biomedical Imaging*, pages 114–123, 2008.

[17] D. Perrone. The effect of gibbs ringing artifacts on measures derived from diffusion mri. *NeuroImage*, 120:441–455, 2015.

[18] E. Kellner. Gibbs-ringing artifact removal based on local subvoxel-shifts. *Journal of Magnetic Resonance*, 76(5):1574–1581, 2016.

[19] M. E. Haacke. Imaging iron stores in the brain using magnetic resonance imaging. *Magnetic Resonance Imaging*, 23(1):1–25, 2005.

[20] Q. Duan. Characterization of a dielectric phantom for high-field magnetic resonance imaging applications. *Medical Physics*, 41(10), 2016.

[21] N. Barrie Smith and A. Webb. *Introduction to Medical Imaging*.

[22] Ma. A. Herráez. Fast two-dimensional phase-unwrapping algorithm based on sorting by reliability following a noncontinuous path. *Applied Optics*, 41(35):7437–7444, 2002.

[23] A. Radoń. Electrical conduction mechanism and dielectric properties of spherical shaped fe_3o_4 nanoparticles synthesized by co-precipitation method. *Materials*, 11(5), 2018.

[24] S. Bagheli. Synthesis and experimental investigation of the electrical conductivity of water based magnetite nanofluids. *Powder Technology*, 274:426–430, 2015.